ADVANCED ENERGY MATERIALS
www.advenergymat.de

Pseudocapacitance Facilitates the Electrocatalytic Reduction of Carbon Dioxide

Juan-Jesús Velasco-Vélez, Axel Knop-Gericke, Beatriz Roldan-Cuenya, Robert Schlögl, and Travis E. Jones**

Electroreduction of CO_2 to value-added products is a promising strategy for CO_2 reuse, where copper has a unique ability to produce oxygenates and C_{2+} products. Unfortunately, the electronic factors making copper so unique are unknown, which limits the ability to design improved catalysts. By combining in situ surface-sensitive X-ray resonant photoelectron spectroscopy with density functional theory calculations, the complex electronic structure of copper is uncovered during the electrocatalytic reduction of CO_2. It is found that the pseudocapacitive charging of copper, produced by the incorporation of protons and electrons into the subsurface, facilitates the activation of CO_2, while simultaneously increasing the barrier for H-H coupling. The net result is that cathodic pseudocapacitive charge suppresses the hydrogen evolution reaction and promotes the production of hydrocarbons and oxygenated products on copper. These results represent a new paradigm in the understanding of CO_2 reduction, highlighting the key role of pseudocapacitive charge in the reaction.

1. Introduction

The interaction of CO_2 with copper is of widespread interest because it controls diverse important processes ranging from (e.g.,) corrosion in pipes[1] to methanol synthesis.[2] Beyond these processes, copper has become the subject of widespread interest because of its unique ability to facilitate the electrochemical reduction of CO_2 to valuable hydrocarbons and alcohols[3] at high Faradaic efficiency under mild conditions.[4] This makes Cu-based catalysts critical in the emerging circular clean carbon economy, where CO_2 and H_2O are the cornerstone molecules[5] that are electro-reduced using renewable energy. The unique ability of copper in electro-reducing CO_2 to valuable C_{2+} products under mild conditions has far reaching impacts for providing feedstocks for the production of pharmaceuticals, plastics, and fuels. Different models have been developed in an effort to explain the uniqueness of copper and its ability to electrochemically produce C_{2+}[6] and oxygenated hydrocarbon products, unfortunately however, a complete description of the electronic factors making copper active in CO_2 reduction remains elusive. Understanding the atomic scale process of CO_2 electro-reduction on copper may allow us to develop more efficient, robust, and selective electrocatalysts for the reduction of CO_2 to valuable oxygenated hydrocarbons and multicarbon products at lower working potentials.[7] To solve this conundrum, in situ characterization of the working copper/electrolyte interface during the cathodic CO_2 reduction reaction (CO_2RR) is necessary. Among the different characterization techniques, X-ray photoelectron spectroscopy (XPS) is the best candidate to accurately measure the electronic structure of copper under electrocatalytic reaction conditions because of its extreme surface sensitivity, especially in comparison to spectroscopic techniques based on photon detection. XPS can provide both surface sensitive and element specific information, as well as detailed information of the ionization potential drop that the ions undergo within the electrical-double-layer (EDL). Measuring these properties is essential if we are to understand the charge distribution near the electrified interface and how the electronic structure evolves with applied potential. Unfortunately, photoelectron based spectroscopic techniques are typically incompatible with gases and liquids; ambient pressure X-ray photoelectron spectroscopy (APXPS) had emerged as a promising technique to overcome this challenge.[8]

J.-J. Velasco-Vélez, A. Knop-Gericke, R. Schlögl
Department of Heterogeneous Reactions
Max Planck Institute for Chemical Energy Conversion
45470 Mülheim an der Ruhr, Germany
E-mail: jvelasco@cells.es

J.-J. Velasco-Vélez, A. Knop-Gericke, R. Schlögl, T. E. Jones
Department of Inorganic Chemistry
Fritz-Haber-Institut der Max-Planck-Gesellschaft
14195 Berlin, Germany
E-mail: tejones@lanl.gov

J.-J. Velasco-Vélez
Experiments Division
ALBA Synchrotron Light Source
Cerdanyola del Vallés, Barcelona 08290, Spain

B. Roldan-Cuenya
Interface Science Department
Fritz-Haber-Institut der Max-Planck-Gesellschaft
14195 Berlin, Germany

T. E. Jones
Theoretical Division
Los Alamos National Laboratory
Los Alamos, NM 87545, USA

The ORCID identification number(s) for the author(s) of this article can be found under https://doi.org/10.1002/aenm.202400054

DOI: 10.1002/aenm.202400054

2. Experimental Section

2.1. Electrode Preparation

Bi-layer graphene (BLG) was purchased from Graphenea (San Sebastian, Spain), model: G/G/Cu/M-25, which was a continuous polycrystalline film supported on copper. The grain size in the range of ≈20 µm, as confirmed by scanning electron microscopy. The copper was eliminated by floating the copper foil on a 100 mM aqueous solution of $(NH_4)_2S_2O_8$ for 24 h in order to assure that the copper support was fully dissolved. The floating BLG was transferred to another beaker filled with Milli-Q water in order to avoid the presence of $(NH_4)_2S_2O_8$ and copper dissolved in the solution. The BLG floating on Milli-Q water was transferred onto a 1 cm wide disk cation exchange membrane (CEM), FKD type sourced from FUMA-Tech GmbH (Bierigheim-Bissingen, Germany), which allows also the transport of water and HO^- groups. The CEM coated with the BLG was dried at room temperature for 24 h. A detailed description of the electro, chemical and mechanical properties of this electrode assembly was discussed by Falling et al..[9] This process leaves a BLG on the FKD membrane, stabilized by van der Waals interaction.[10] The study used an EC-cell based on an ion conductive membrane upgraded to be used with a transparent 2D working electrode (graphene), which allows better wetting of the sample, while retaining an appropriate escape depth of the photoelectrons than a cell without graphene. A continuous flow of 50 mM $CuSO_4$ (4.3 pH) was passed through the cell, in order to accomplish the electrodeposition of copper on the graphene electrode at −1.6 V versus Ag/AgCl. Finally, the $CuSO_4$ electrolyte was flushed out with pure water and the water was replaced by 100 mM $KHCO_3$ (saturated with CO_2). A detailed description of the X-ray beam effects on these membranes and how it can be minimized can be found elsewhere.[11] Note that the spectra shown in **Figure 1** were collected in the same point, meanwhile the spectra shown in Figure S2 (Supporting Information) were collected in fresh spot for each potential. Both experiments showed the same trends indication that the beam effect are not present/dominant in the reported spectra. During the CO_2RR measurements, the main APXPS chamber was filled with 0.5 mbar of CO_2.

The Au electrode was fabricated by sputtering Au onto the FKD membrane. After that a BLG graphene was transferred onto the sputtered Au/FKD assemble following the same approach as described above. It produces a "sandwiched" Au electrode between the FKD and graphene membranes.

2.2. In Situ Flow Cells

The in situ electrochemical flow liquid cell was operated in the main chamber of the innovative station for in situ spectroscopy (ISISS) beamline in BESSY II (Berlin, Germany). The ISISS beamline was equipped with a SPECS PHOIBOS 150 NAP hemispherical analyzer sourced by SPECS Surface Nano Analysis GmbH (Berlin, Germany). The main body of the electrochemical cell was made of polyether ether ketone (PEEK),[12] which was electrically insulator and chemically inert. The counter electrode was a Pt wire, and the reference electrode was a Ag/AgCl FLEXREF sourced from World Precision Instruments (Florida, USA). The electrolyte flow was maintained with a peristaltic

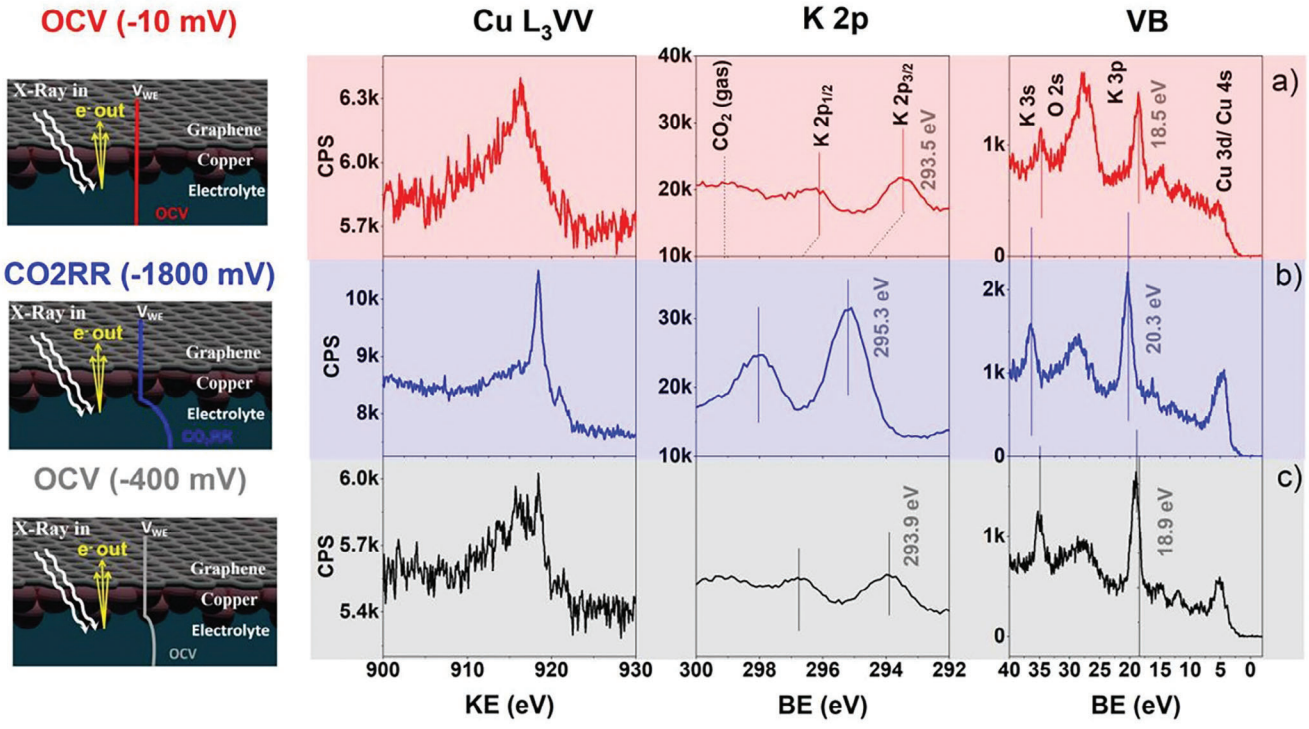

Figure 1. Spectroscopic measurements at the electrical double layer: Cu L_3VV, C 1s, and VB spectra collected depending on the applied potential in presence of 100 mM $KHCO_3$ saturated in CO_2. A) OCV (−10 mV), B) CO_2RR (−1.8 V vs Ag/AgCl), and C) OCV (−400 mV) after CO_2RR.

pump PERIMAX 16- Antipuls sourced from SPETEC GmbH (Erding, Germany).

2.3. Electrolytes

As mentioned above, the copper electrode was prepared by electrodeposition of copper from a 50 mM $CuSO_4$. This electrolyte was prepared by diluting 7.98 g of $CuSO_4$ (Sigma Aldrich, anhydrous powder, 99.99%) in 1 liter of Milli-Q water (18.2 MΩ) at room temperature (RT), 25 °C, saturated in pure N_2 gas. The 100 mM $KHCO_3$ used in CO_2RR measurements was prepared by diluting 10 g of $KHCO_3$ (Roth, 99%) in 1 liter of Milli-Q water (18.2 MΩ) at room temperature, 25 °C; it was saturated with pure CO_2 by bubbling the electrolyte. The 100 mM H_2SO_4 (pH ≈1) was prepared by diluting 9.8 g of H_2SO_4 (purity 98%, Alfa Aesar, Massachusetts, USA) in 1 liter of Milli-Q water (18.2 MΩ) at room temperature and saturated with pure N_2 gas by continuously bubbling.

2.4. Potentiostat

Potentiometric control was assured with a SP-300 Biologic (Seyssinet-Pariset, France), allowing for different potentiometric and amperometric controls.

2.5. ResPES Cu^{2+}, Cu^{+}, and Cu^{0} References

The Cu^{2+} and Cu^{+} reference materials were prepared by oxidizing a copper foil in the presence of 0.5 mbar O_2 at 400 °C and 200 °C, respectively. A metallic reference, Cu^0, was prepared by heating a copper electrode in 0.5 mbar H_2 at 400 °C. The desired oxidation state of the sample was checked by in situ spectroscopy using the ISISS APXPS end station in BESSY II (Berlin, Germany). The ResPES valence band maps were collected using photon energies in the vicinity of the Cu2p absorption edges in order to correlate the Cu2p transitions to the unoccupied 3d and 4sp orbitals with the valence band states. Figure S1 (Supporting Information) shows the color maps of the valence band photoemission spectra through the Cu L_3 ($Cu2p_{3/2}$) absorption edges of three different materials (Cu^{2+}, Cu^{+}, and Cu^0). By doing so, the electronic structure of the different copper (oxides) is shown:

i. Cu^{2+} ResPES: The off-resonant photoemission spectra taken below the Cu L_3-edge white line (Figure S1C, Supporting Information) indicates the existence of a main peak at around 2–6 eV (Cu3d peak) and a satellite peak at around 8–16 eV. Going toward the Cu L_3-edge white line, the satellite increases in intensity, reaching its maximum at the white line energy of the Cu L_3 edge (Cu^{2+} maximum of the white line). The intensity decreases at higher photon excitation energies beyond the white line energy and the regular L_3VV Auger signal appears where the off-resonance photoemission was recovered. The resonant process in Cu^{2+} was controlled by two different photoemission channels: The direct photoemission channel $3d^9+h\nu \rightarrow 3d^8+e$ and the photoabsorption process follows by a super Coster-Kronig Auger decay ($np^63d^9+h\nu \rightarrow np^53d^{10} \rightarrow np^63d^8+e$) *(34)*. As the 3d direct emission represents a $3d^{n-1}$ final state in transition-metal oxides, the satellite can be described as an intra-d-band shake up process, which satisfied the monopole selection rules ($\Delta s = \Delta l = 0$)[13] required for shake-up processes at higher photon energies. These transitions are not due to a transition from a ligand oxygen (O2p) to an emptied 3d metal but due to allowed intra-d-shell excitation with unfilled d states (3d open shell).
ii. In the case of the Cu^{+} oxide, the satellite peak increases its intensity reaching its maximum with the energy of the maximum white line intensity of the Cu L_3 edge (Figure S1B, Supporting Information). The Cu^{+} oxide had a formally close 3d band. Consequently, transitions to the $3d^8$ final state should not be visible in the one electron removal spectrum, unless the final state is $3d^84(sp)^1$. This state can be only reached because the ground state of Cu_2O hybridized the 3d and 4(sp) shells, where the Cu4(sp) and $3d(3z^2\text{-}r^2)$ orbitals combine with the $O2p_z$ orbitals of the neighboring oxygen atoms,[14] highlighting the importance of the O2p—Cu4(sp) hybridization in the overall process description.
iii. Finally, for Cu^0 the existence of a formally close 3d band results in a resonant peak at the energy of the maximum of the Cu L_3 edge (Figure S1A, Supporting Information), which was ascribed to the existence of 3d closed shell following the same trend as the Cu^{+} oxide. Other studies suggested a $d^{9.x}$ ground state because of the transfer of d electron density to the coherent band at the Fermi edge,[15] thus when a d^{10} state is reached the white line intensity drops. The s character appears in the $L_{2,3}$ edges at the same energy as the d orbitals because of hybridization, but the s cross-section was low. Because of that, it was more correct call the $d^{9.x}$ state d^{10} rather than d^9.

2.6. DFT Calculations

All density functional theory (DFT) calculations were performed with the Quantum ESPRESSO package[16] using the Perde-Burke-Ernzerhof (PBE) exchange and correlation potential with projector augmented wave (PAW) datasets from the pseudopotentials (PPs) library[17] using a kinetic energy cutoff of 60 Ry and a charge density cutoff of 480 Ry. A **k**-point mesh equivalent to (20 × 20) for the (1 × 1) surface was used for Cu(001) surfaces with cold smearing using a smearing parameter of 0.01 Ry. Cu(001) was chosen as it was more selective to C_{2+} and was the dominant facet on polycrystalline samples under CO_2RR conditions.[18] Slabs were modeled using ten-layers with 25 Å vacuum separating periodic images. Phase diagrams were computed using the computational hydrogen electrode including the zero point energy (ZPE) of H, which was computed for H dissolved in the octahedral hole of a (2 × 2 × 2) crystallographic supercell of the crystallographic unit cell and for 1/16 monolayer (ML) H adsorbed on the hollow site of Cu(001). Changes in H coverage or placing H in substitutional sites changed the computed ZPEs by <0.05 eV and thus were not considered as such minor differences will not alter the predictions. X-ray absorption spectra (XAS) were computed by solving the Bethe-Salpeter equation with the OCEAN package[19] using normconserving pseudopotentials with a kinetic energy cutoff of 120 Ry and including

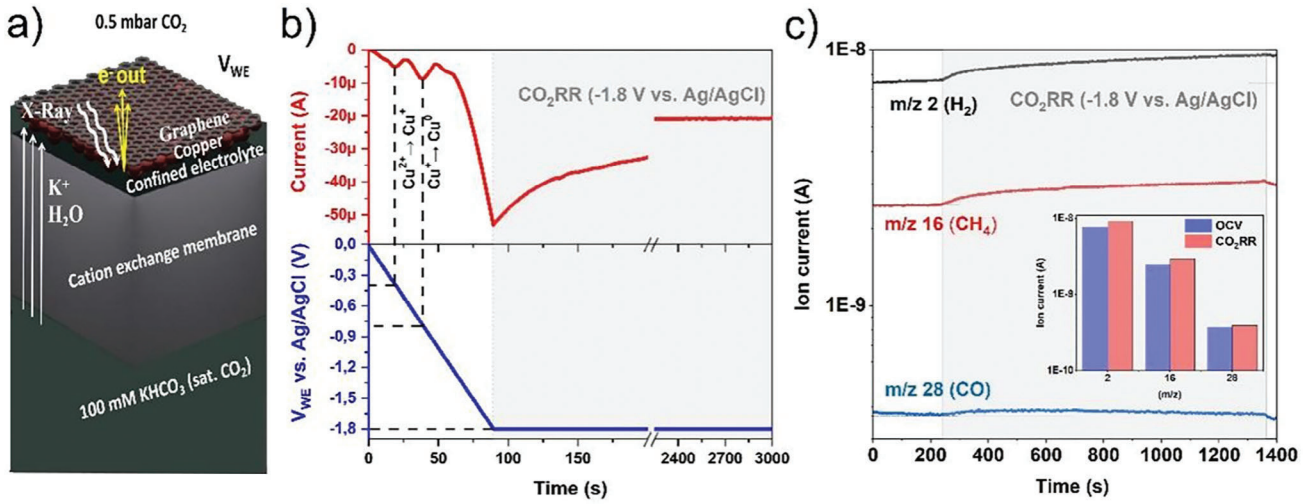

Figure 2. A) Schematic representation of the detection scheme and potential drop under B) Linear sweep voltammetry (LSV) collected from OCV up to −1.8 V versus Ag/Cl (scan rate 20 mV s^{-1}) followed by chronoamperometry under CO_2RR conditions (−1.8 V vs Ag/AgCl) collected with the copper electrodeposited onto the graphene current collector electrode. C) QMS measurements of H_2 (m/z 2), CO (m/z 28), and CH_4 (m/z 16) products evolving during the CO_2RR proving the catalytic activity of the electrode assembling.

empty states to over 100 eV above the threshold. XAS alignment was accomplished through delta self-consistent (ΔSCF)[20] calculations using Quantum ESPRESSO, with the bulk metal aligned to experiment. The Auger spectra were computed using Cini-Sawatzky theory with a U_{dd} of 7 eV for bulk species and 7.5 eV for surfaces.[21] The Auger contribution to the resonant photoemission spectroscopy (ResPES) were modeled using the computed Auger and XAS spectra. For computational efficiency, activation energies were computed using 5-layer slabs and solvent effects were modeled using a self-consistent charge solvation model for water.[22] The electrochemical potential of the simulations was held fixed at −1.8 V versus Ag/AgCl using the effective screening medium method.[23] Transition states were found using the climbing image nudged elastic band method using 8–10 images to discretize each path with a single transition state on each path. O1s spectra were computed using the ΔSCF method with (4 × 4) slabs, where a (4 × 4 × 4) supercell of Cu_2O was used for the O1s reference assuming a binding energy of 532 eV. To estimate the O1s binding energy of CO_2 in the EDL, DFT based molecular dynamics was used to capture explicit solvent effects by introducing water into the vacuum region between slabs and equilibrating for ≈5 ps at 350 K using a Berendsen thermostat with $dt/\tau = 1/50$ and a 1 fs timestep.

3. Results and Discussion

We investigated the electronic structure of a copper electrode during the electrocatalytic CO_2RR using the APXPS endstation located at the innovative station for in situ spectroscopy (ISISS) beamline in BESSY II (Berlin, Germany).[24] Note that APXPS is not readily compatible with liquids, and requires sophisticated technical approaches for its operation under aqueous conditions,[12b,25] including, combining the use of APXPS with photoelectrons of high kinetic energies (thousands of eV)[25] to allow the photoelectrons to escape from a thin film electrolyte (up to few nanometers thick). Alternatively, ultra-thin membranes (i.e., graphene) that are transparent to the photoelectrons[26] allow measurements in the soft X-ray regime, though such membranes are prone to mechanical failure. An intermediate solution was recently developed in our group[11,27] involving the use of ionomer membranes[28] and later upgraded to incorporate a graphene membrane. As with a graphene-membrane cell,[29,30] the graphene is transparent to low energy photoelectrons, thereby ensuring higher surface sensitivity than when harder X-rays are used. However, by supporting graphene on an ionomer membrane, the detrimental effects of holes that may form in the graphene are minimized. Thus, combing graphene with an ionomer membrane cell[28] offers a mechanically robust way to achieve high surface sensitivity in situ measurements. Such surface sensitive information is critical for probing catalytic reactions. Graphene also acts as a current collector and evaporation barrier to allow the formation of confined liquid electrolytes, which improves the performance of in situ electrocatalytic APXPS.[9] Technical details of the in situ setup used in this investigation are shown in the experimental section. Following this approach, the detection scheme is shown in **Figure 2A**.

A detailed description of the electronic structure of copper under CO_2RR conditions requires us to measure the outer shell orbitals that mediate the interaction between copper, oxygen, and hydrogen. In particular, we are interested in charge transfer between the Cu3d and the O2p orbitals of the H_2O and CO_2 molecules and any intermediates. To investigate this, a copper electrode was electrodeposited from 50 mM $CuSO_4$ onto the surface of a graphene electrode following the procedure described in the experimental section.[11,31] Figure 2B shows the electrochemical performance of such electrodeposited copper in the presence of 100 mM $KHCO_3$ (saturated in CO_2 and with 0.5 mbar CO_2 partial pressure in the experimental APXPS main chamber). The linear sweep voltammetry (LSV) in Figure 2B shows two reduction waves that can be ascribed to the transitions from

Cu^{2+} to Cu^{+} and from Cu^{+} to Cu^{0}. Under CO_2RR conditions (−1.8 V vs Ag/AgCl) the current is constant, indicating the expected performance of this approach under steady state operation. The catalytic activity of the electrode assembly is probed by on-line quadrupole mass spectrometry (QMS), where we monitor the masses of H_2 (m/z 2), CO (m/z 28), and CH_4 (m/z 16) evolving from the electroreduction of CO_2 (Figure 2C). Under open circuit voltage (OCV), −10 mV versus Ag/AgCl, the copper electrode is in a mixed Cu^{2+}/Cu^{+} oxidation state, which can be seen in the Cu LMM Auger spectra, see Figure 1A.[32] Once the electrode is polarized to −1.8 V versus Ag/AgCl, (CO_2RR conditions), the copper electrode undergoes reduction to metallic copper,[33] as shown in Figure 1B. Note that the shift observed in the K2p position corresponds to the −1.8 V versus Ag/AgCl applied to the electrode due to the potential drop within the EDL. Under these conditions the Auger spectrum indicates that copper is reduced. This process is reversible, as shown in Figure 1C. Furthermore, the valence band (VB) spectra measured in situ shows the K3p and K3s spectra shift to higher BE with the higher applied potential. Further inspection of the in situ VB reveals the K3p and K3s peaks increase in intensity, revealing that K^{+} cations accumulate at the interface to form the EDL. Thus, we can confirm that the Cu3d spectra were collected at the electrified catalyst/EDL interface. That is, under these conditions, the number of electrons changes such that the Fermi level of the metal matches the applied potential, and this excess surface charge is neutralized by the electrolyte ions accumulated within the EDL (total charge neutrality conditions) to capacitively charge the electrode. And though this capacitive charging leads to surface charge densities only on the order of $\mu C/cm^2$, we can observe the charging in XPS through its direct influence on the position of the K^{+} 3p line relative to the charged surface. These results demonstrate the electrochemical cell performs correctly during the CO_2RR and the spectra collected under reaction conditions capture the electronic structure of the operating copper electrode. A scheme of the potential drop under different applied potential is shown in Figure 1. Note that the quantification of the products evolving from the CO_2RR are difficult to quantify with the on-line QMS measurements. Furthermore, it is not possible to perform on-line gas chromatography (GC), which is a more suitable technique for the quantification of products: This limitation is due to the fact that the water vapor (present in the experimental chamber) will condense in the columns of the GC as it is pressurized to the atmospheric pressure required for the operation of the GC, which will damage the device.

While the observed double layer charging is expected, XPS further reveals chemical modification of the electrode surface occurs coincident with EDL formation. Under the CO_2RR potential the Cu3d peak intensity is increased compared to OCV, which requires charges far in excess of those achieved through capacitance. Removing the applied potential and going back to OCV (−400 mV vs Ag/AgCl) results in a decrease in intensity of the Cu3d VB spectra due to the re-oxidation of copper. Furthermore, Figure S2 (Supporting Information) shows the change in the Cu3d VB and Cu L_3-absorption-edge peak intensity with the cathodic potential, where further reduction at higher cathodic polarization was seen at the Cu L_3-edge, in total electron yield (TEY) mode, in good agreement with previous results.[11] Similarly, the Cu3d orbitals in the VB close to the Fermi edge show increased intensity at higher cathodic polarization, which indicates the clear influence of the applied potential on the density of Cu3d electrons under higher cathodic potentials. However, the combined changes in the EDL and surface chemistry limit our ability to understand how the applied potential influences the electronic structure of copper from the VB and Auger spectra alone.

To understand the observed changes in the electronic structure at the electrified interface at cathodic potentials, as well as identify the presence of active/intermediate species, we performed in situ ResPES under electrocatalytic reaction conditions. ResPES provides a unique means of identifying the character of various states involved in the electrocatalytic CO_2 reduction. **Figure 3A** shows the ResPES color map of the valence-photoemission as the photon energy is tuned across the Cu L_3-edge (in the vicinity of the $Cu2p_{3/2}$ core level). In the case of the ResPES map collected through the Cu L_3-edge,[13,34] full range Auger electron yield (AEY) is shown on the top of the figure. Integrating the full range of binding energies can be seen to accurately reproduce the Cu^{2+}/Cu^{+} AEY XAS, see the red spectrum on the top of Figure 3A, where a mixed Cu^{2+}/Cu^{+} oxide is observed, in agreement with the XP/Auger spectra shown in Figure 1.

The ResPES map contains additional information beyond the AEY since the binding energy of photoelectrons are simultaneously resolved. First consider the photoemission peak at 17.7 eV binding energy in Figure 3A that appears across all excitation energies. This peak is the K3p and is ascribed to the K^{+} ions (of the 100 mM $KHCO_3$ electrolyte) in the EDL, its presence makes it possible to record AEY spectra (full range spectra) at the same time that the applied potential is tracked using the shift in the K3p peak position of the K^{+} in the EDL. When a potential of −1.8 V versus Ag/AgCl is applied, the K3p peak position is shifted to 19.5 eV, as shown in Figure 3B, demonstrating the potential drop across the EDL is captured. Further information can be gained when the photoemission spectra at specific excitation energies are examined because resonance requires localized holes in the initial state, a $3d^9$ initial state for Cu^{2+}[35] (references are shown in Figure S1, Supporting Information). To see this, consider that in the pre-edge region, the regular L_3VV Auger signal is observed, thereby recovering the off-resonance photoemission. Increasing the excitation energy toward the white line energy leads to an increase in the satellite intensity at 13.9 eV, Figure S3 (Supporting Information). Such a giant resonance is associated with a $3d^8$ final state of Cu^{2+}.[34,36] Consistent with this picture, the 13.9 eV satellite reaches its maximum at the white line energy of the Cu^{2+} edge (931 eV excitation energy shown in Figure S3B, Supporting Information). As the excitation energy approaches the energy of the maximum of the Cu^{+} white line (934 eV excitation energy shown in Figure S3E, Supporting Information), a higher energy satellite (15.8 eV) reaches its maximum value. This satellite can be assigned to a $3d^8$ final state associated Cu^{+}; it is at higher energy than the CuO satellite due to the cost of exciting a 3d electron to the 4sp shell of Cu^{+}, as previously noted.[14a,36] The intensity of these satellites decreases at photon energies beyond the energy corresponding to the white line in the XAS, and the off-resonance photoemission and Auger spectra are again recovered. Thus, the complex structure seen in Figure 3A is a consequence of the presence of different oxides, Cu^{2+}/Cu^{+} (see Figure S1, Supporting Information, for references the ResPES color maps of Cu^{2+}, Cu^{+} and Cu^{0}).

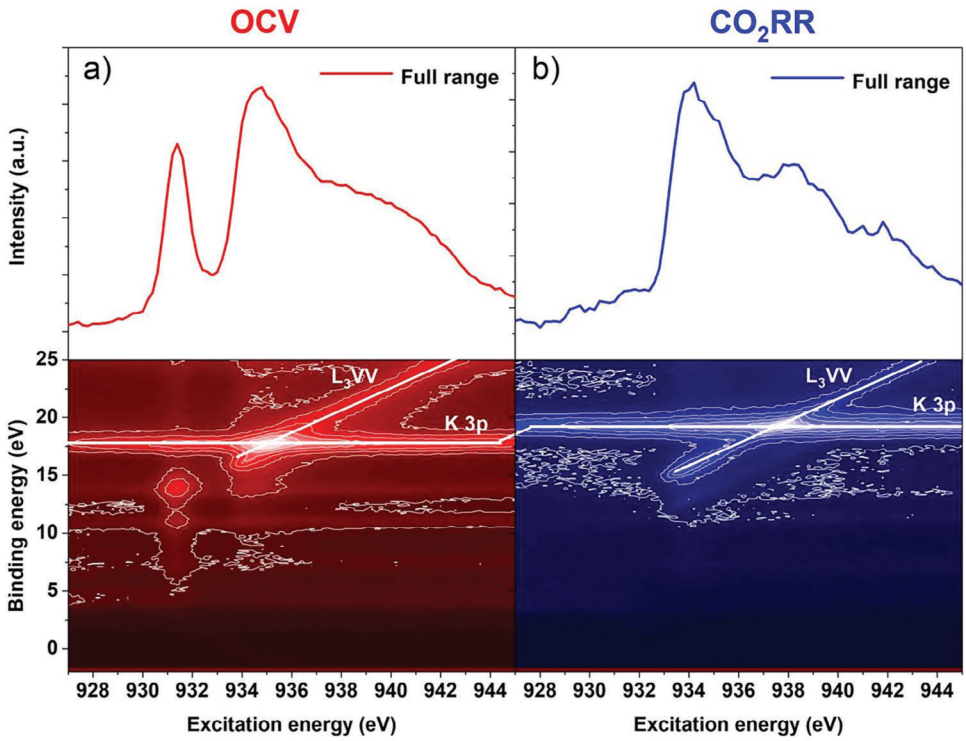

Figure 3. ResPES Color maps of the valence-band photoemission spectra through the Cu L_3 ($Cu2p_{3/2}$) collected under A) OCV and B) CO_2RR conditions.

Figure 3B show the ResPES color maps at the Cu L_3-edge under CO_2RR conditions (−1.8 V vs Ag/AgCl). The potential can be seen to shift the K3p peak by ≈1.8 eV, indicating the correct potential drop across the EDL and the correct electrochemical performance of the cell. Under these conditions the electrode can also be seen to undergo reduction to metallic Cu, as seen in the non-resonant Auger/VB spectra, and the full ResPES map, see Figures S4 and S5 (Supporting Information). This results in a formally closed Cu3d band, where the ResPES map shows a resonant peak at the energy associated with the white line of the Cu L_3-edge (excitation energy 934, Figure S3E, Supporting Information) consistent with the two-hole $3d^8$ final state of Cu^0.[37] The full range AEY (top graphic, blue spectra in Figure 3B) resembles the Cu L_3-edge spectra of metallic copper collected in TEY and AEY modes, although the resonance at 942 eV has practically vanished, indicating copper with reduced 3d bandwidth[38] and/or a small partial positive charge. While EDL capacitive charging is unable to produce these observed chemical changes, such copper species can form when the electrode is pseudocapacitively charged through the dissolution of protons and electrons into the lattice. From DFT, this pseudocapacitive charging is predicted to become thermodynamically favored at potentials cathodic of ca. −0.8 V versus Ag/AgCl. XAS simulations show the resulting copper species have the experimentally observed spectral fingerprint (Figure S6, Supporting Information). Once dissolved, hydrogen favors the formation of vacancy-H complexes through the super abundant vacancy (SAV) mechanism,[29] with DFT predicting Cu_3VacH_x clusters (x = 1–6) to be metastable under CO_2RR conditions, see Figure S7 (Supporting Information). The XA spectra of these SAVs are in excellent agreement with the measured absorption spectrum, Figure S6 (Supporting Information), showing the reduction in the resonance at 942 eV without significant modification of other spectral elements. Because collection of the photoelectrons allows us to confirm the correct applied potential (i.e., monitoring the K3p peak), which is not possible with conventional XAS, we can be certain the applied potential is sufficient to drive SAV formation. Moreover, the PES data from ResPES allows further verification of this assignment. Beyond XAS, the resonant photoemission in the color map reaches its maximum at the energy associated with the white line maximum of the Cu L_3-edge at an excitation energy of 934 eV (Figure S3E, Supporting Information), the intensity decreases at higher photon energies, where the regular L_3VV Auger signal appears, and the off-resonance photoemission is recovered. The most intense ^1G peak appears at ≈15 eV binding energy at resonance, making the spectrum under CO_2RR conditions similar to that found for metallic copper in ultra-high-vacuum (UHV) or under H_2 at 400 °C (Figures S1A and S5, Supporting Information) indicating copper retains a formally closed 3d band under CO_2RR conditions.[14b]

It is noteworthy that the surface sensitivity of ResPES (the inelastic mean free path of the photoelectrons is ca. 15 Å) makes it possible to examine the types of subsurface species present during CO_2RR, which are expected to influence the catalytic performance.[15,30] While the closed 3d band suggests oxidized copper is not present under CO_2RR conditions, when comparing the computed XAS (Figure S6, Supporting Information) with experiment, it is unclear if dissolved O is present from XAS alone. From the computed full ResPES map, however, we see that oxygen in the subsurface would appear at low excitation and binding

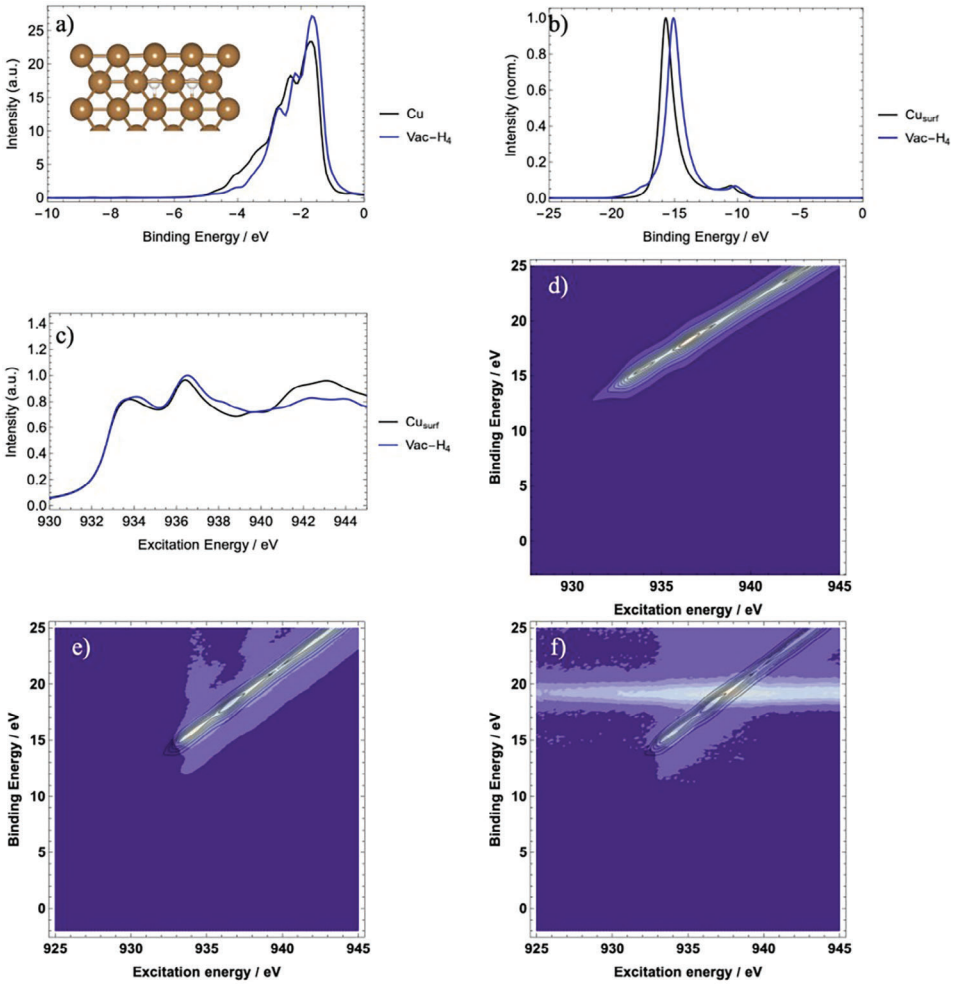

Figure 4. a) Computed projected density of states, b) Auger at resonance, c) Cu L_3-edge absorption spectra, and d) computed ResPES of Cu in a H-induced subsurface vacancy cluster. Heat map of ResPES measured under H_2 at 400 °C with the H-induced subsurface vacancy cluster calculation overlaid (e). Heat map of ResPES measured under CO_2RR conditions with the H-induced subsurface vacancy cluster calculation overlaid (f).

energy regions in the map, where it could be distinguished from metallic copper (Figure S8, Supporting Information). This lack of oxidized copper is expected from thermodynamic considerations. The computed Cu(001) surface phase diagram (Figure S9, Supporting Information) shows bulk hydride (CuH) is the stable phase solid-phase at −1.8 V versus Ag/AgCl, though computation of the VB and ResPES demonstrate there is no evidence for CuH formation under CO_2RR conditions (Figure S10, Supporting Information); the absence of hydride is consistent with the formally closed 3d band. Thus, hydrogen consumption through the hydrogen evolution reaction (HER) and CO_2RR trap the system in a metastable state. Inspection of the computed surface phase diagram for Cu(001) (Figure S9, Supporting Information) reveals that high coverages of adsorbed hydrogen are the thermodynamically favored metastable near-surface phases, including a well-studied H-induced $(2\sqrt{2} \times 2\sqrt{2})$R45° surface reconstruction.[39] The computed ResPES, however, shows such phases disagree with the measurements (Figure S11, Supporting Information). Thus, as a final possibility, we considered metastable subsurface H-induced SAV phases like those considered in the bulk. Like their bulk counterparts, subsurface Cu_3VacH_x clusters are metastable (Figure S9, Supporting Information), and they yield computed spectra in agreement with the experiments. Taking the Vac-H_4 phase as a representative example, we see that the computed ResPES maps, XAS, and resonant Auger of subsurface SAVs produced through pseudocapacitive charging is in agreement with the spectra measured during CO_2RR (**Figure 4**). In particular, the surface copper atoms show a suppression of the resonance ≈943 eV in the Cu L_3-edge together with the increase in VB intensity near the Fermi energy observed during CO_2RR. Thus, SAV formation is a mechanism for cathodic pseudocapactive charge storage in Cu electrodes.

In order to determine the reaction pathway and possible role of SAVs and pseudocapacitive charge storage, the copper electrode performance was compared with an Au electrode sputtered onto the ionomeric membrane capped with a graphene layer as a control experiment, which allowed us to contrast the formation of intermediates during electrocatalytic CO_2 reduction on Cu and Au

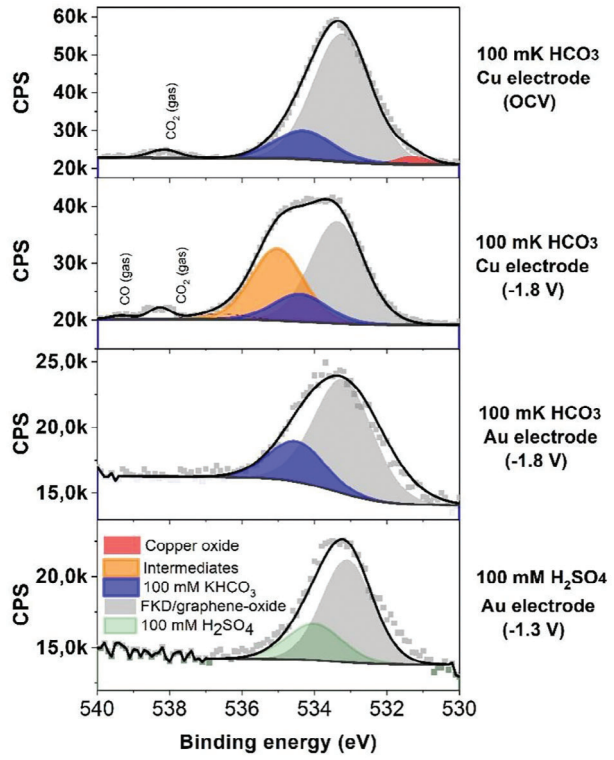

Figure 5. O1s spectra collected for different working electrodes (Au and Cu) in presence of 100 mM $KHCO_3$ (saturated in CO_2) or 100 mM H_2SO_4 saturated in N_2 at different potentials.

(the electrode preparation is described in the experimental section). The electrochemical performance of the Au electrode and the variation in the Au4f and VB depending on the applied potential is shown in Figure S12 (Supporting Information) in the presence of 100 mM H_2SO_4 saturated in N_2 and 100 mM $KHCO_3$ saturated in CO_2. No changes in the VB spectra of Au were detected under cathodic polarization indicating no variations in the valence 5d band as a function of the applied cathodic potential (in the presence of 100 mM $KHCO_3$ saturated in CO_2). Note that the variation in the K3p peak with applied potential indicates the correct potential drop within the EDL for the Au electrode assembly (Figure S12C, Supporting Information). The nature of possible intermediate oxygenates was further investigated by comparing the in situ O1s spectra measured on Cu and Au electrodes, as shown in **Figure 5**. These spectra were collected at 600 eV kinetic energy, a discussion on the depth sensitivity with this assembly can be found elsewhere.[40] Only Cu shows possible reaction intermediates. The fitting parameters used for the spectra analysis are shown in Table S1 (Supporting Information). We assign the species at 531.1 eV to Cu_2O (see Figure S13, Supporting Information, for references), while the computed O1s binding energies suggest that CO_2 on a surface with adsorbed or subsurface H accounts for the intermediates seen on Cu during CO_2RR (see Table S2, Supporting Information, for species assignment). Note that the peaks at 533.1 eV and 534.5 eV are ascribed to the membrane electrolyte species containing oxygen, which were extracted from the comparison with the Au electrode. The lack of variation in the Au5d band may be linked to the inability of Au to form an SAV phase and pseudocapacitively charge under CO_2RR conditions; DFT shows the thermodynamics of SAV formation in Au require potentials 1 V beyond those associated with Cu. The lack of pseudocapacitive charge in Au leads to different reaction pathways for CO_2 electroreduction on gold, which leads to CO formation, whereas over copper, multicarbon and oxygenated products are formed.[4,41] This result indicates that high coverages of CO_2RR intermediates cannot be adsorbed easily on the Au surface due to its unaltered valence band and low reactivity. Still, the lack of strongly bound intermediates on the copper surface suggests CO_2 activation remains rate limiting even on the activated copper electrode. To gain insight into this kinetic limitation, we computed minimum energy paths for CO_2 activation on the Cu surfaces considered in this work.

Beginning with a surface with adsorbed H we find that carboxylate formation is slow compared CO_2 activation on the bare metal surface, with apparent activation energies (E_{app}) of 1.24 and 1.00 eV, respectively, see Figure S14 (Supporting Information). These E_{app} are more than the 0.83 eV associated with H_{ads} recombination, suggesting a relatively high HER rate compared to CO_2RR on such a surface through these competing mechanisms. Subsurface H, however, significantly lowers the barrier for CO_2 activation through pseudocapacitive charging of the copper surface. When dissolved interstitially, subsurface H can reduce E_{app} for CO_2 activation to 0.70 eV, see Figure S15 (Supporting Information); subsurface H simultaneously increases the barrier for H-H coupling to 1.00 eV, which may suppress the parasitic hydrogen evolution. When the thermodynamically favored H-induced SAVs form, the increased pseudocapacitive charge leads to a further reduction in E_{app} for CO_2 activation to 0.45 eV (**Figure 6**), which will result in an increase in the surface oxygenate coverage required to produce the multicarbon and oxygenated reaction products that are not easily accessible through gas-phase chemistry or through the use of other elements, such as Au, due to the lack of pseudocapacitive charge capable of easily activating CO_2 and limiting H-H coupling. Such pseudocapacitive charge storage may then appear in more complex systems and other reactions; thus these findings and the presented approach then open new possibilities to understand and investigate more complex systems alloy electrodes[42] and ionomer/electrode interactions[43] as well as different hydrogenation reactions as ammonia synthesis.[44]

4. Conclusion

In summary, we found that the formation of multicarbon and oxygenated hydrocarbon species are facilitated at a copper/electrolyte interface by the reduction of the copper surface and elimination of adsorbed O/OH species; pseudocapacitive charge storage facilitates the activation of CO_2 on copper while H-H coupling remains limited due to the formally closed Cu3d band. Therefore, the electrocatalytic reaction pathways to hydrocarbons observed on copper occur on a clean surface devoid of oxygen species, highlighting the fact that copper can electroreduce CO_2 in the absence of oxidized copper. Conversely, pseudocapacitive charging was not found in Au electrodes that electroreduce CO_2 to CO, thereby demonstrating both the importance chemical reduction of catalyst surfaces has on product selectivity

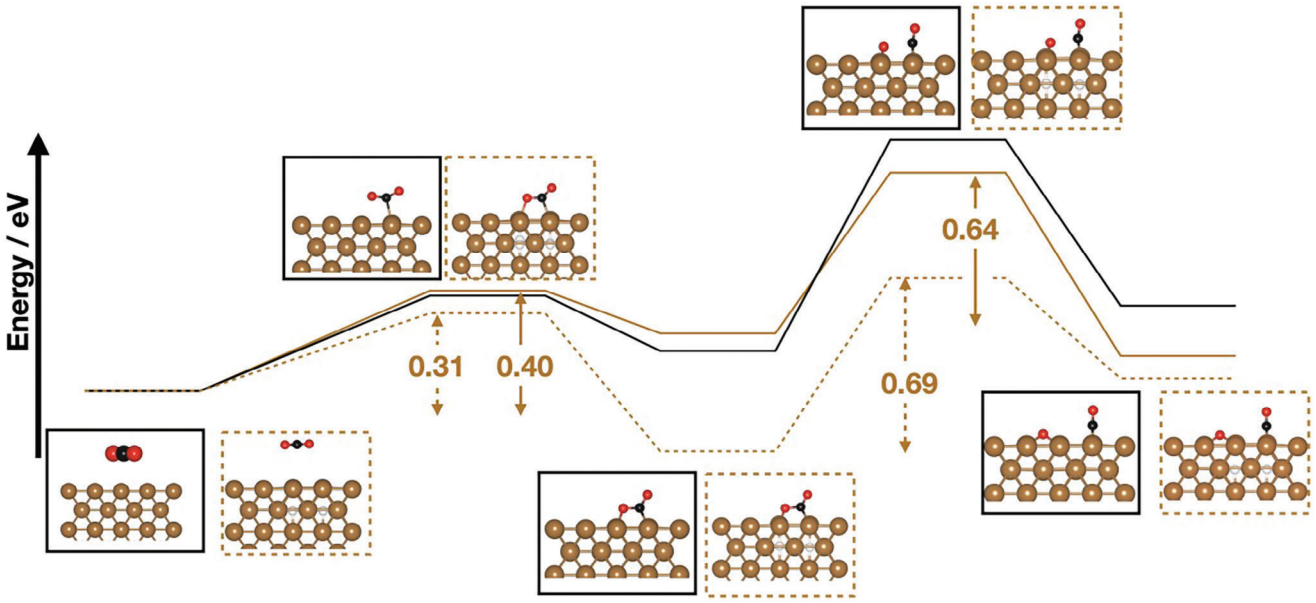

Figure 6. DFT calculations: Minimum energy paths for the C—O bond breaking on Cu(001) with a subsurface H_4-vacancy cluster (dashed), giving ¼ ML total H coverage, and the same structure without the Cu subsurface vacancy (solid). The subsurface H_4-vacancy complex can be seen to result in a reduction in the barrier for CO_2 adsorption/activation compared to the same surface without a Cu vacancy and the clean surface. The barrier for C—O bond breaking is also reduced by subsurface H, with the H_4-vacancy complex (0.69 eV) showing a higher barrier for the elementary step than the same subsurface without Cu subsurface vacancy (0.64 eV). At only 0.45 eV, the apparent activation energy (defined as the highest barrier relative to the initial state) is lowest for the subsurface H_4-vacancy cluster, as compared to 0.87 eV in the absence of the vacancy and 1 eV for the clean surface.

and the need for *operando* spectroscopic methods for identifying such chemical changes.

Received: January 4, 2024
Revised: May 12, 2024
Published online:

Supporting Information

Supporting Information is available from the Wiley Online Library or from the author.

Acknowledgements

The authors thank the Helmholtz-Zentrum Berlin für Materialien und Energie for allocate beamtime for the experiments within the proposal numbers 192–08521 and 191–08014. The authors thank High Performance Computing Center Stuttgart for computational time. T.E.J. thanks the Laboratory Directed Research and Development program of Los Alamos National Laboratory under project number 20240061DR for support.

Open access funding enabled and organized by Projekt DEAL.

Conflict of Interest

The authors declare no conflict of interest.

Data Availability Statement

The data that support the findings of this study are available from the corresponding authorsc upon reasonable request.

Keywords

carbon dioxide, copper electrode, DFT calculations, electrocatalysis, in situ/operando photoelectron spectroscopy

[1] M. Edwards, *J. Am. Water Works Assoc.* **1996**, *28*, 81.
[2] M. Behrens, *Science* **2012**, *336*, 893.
[3] a) Y. Hori, *Chem. Lett.* **1985**, *14*, 1695; b) Y. Hori, *Chem. Lett.* **1986**, *15*, 897.
[4] A. A. Peterson, *J. Phys. Chem. Lett.* **2012**, *3*, 251.
[5] a) R. Schlögl, *Green* **2012**, *2*, 1; b) E. V. Kondratenko, *Energy Environ. Sci.* **2013**, *6*, 3112.
[6] Y. Zheng, *J. Am. Chem. Soc.* **2019**, *141*, 7646.
[7] a) D. Raciti, *ACS Energy Lett.* **2018**, *3*, 1545; b) D. Gao, *Nat. Catal.* **2019**, *2*, 198; c) S. Nitopi, *Chem. Rev.* **2019**, *119*, 7610; d) Y. Y. Birdja, *Nat. Energy* **2019**, *4*, 732.
[8] M. Salmeron, *Surf. Sci. Rep.* **2008**, *63*, 169.
[9] L. J. Falling, *ACS App. Mater. Interfaces* **2020**, *12*, 37680.
[10] a) J. J. Velasco-Velez, *J. Phys. Chem. C* **2014**, *118*, 25456; b) J. J. Velasco-Velez, *J. Electrochem. Soc.* **2013**, *160*, C445.
[11] J. J. Velasco-Velez, *ACS Energy Lett.* **2020**, *5*, 2106.
[12] a) J. J. Velasco-Vélez, *J. Phys. D: Appl. Phys.* **2021**, *54*, 124003; b) J. J. Velasco-Vélez, *Faraday Discuss.* **2022**, *236*, 103.
[13] M. R. Thuler, *Phys. Rev. B* **1982**, *26*, 669.
[14] a) J. Ghijsen, *Phys. Rev. B* **1990**, *42*, 2268; b) Z. X. Shen, *Phys. Rev. B* **1990**, *42*, 8081.
[15] J. Luitz, *Eur. Phys. J.* **2001**, *21*, 363.
[16] P. Giannozzi, *J. Phys.: Condens. Mater.* **2009**, *21*, 395502.
[17] N. Ru, *Phys. Rev. B* **2006**, *73*, 033101.
[18] a) K. J. P. Schouten, *J. Am. Chem. Soc.* **2012**, *134*, 9864; b) Y. G. Kim, *Langmuir* **2014**, *30*, 15053.

[19] a) K. Gilmore, *Comput. Phys. Commun.* **2015**, *197*, 109; b) J. Vinson, *Phys. Rev. B* **2011**, *83*, 115106.
[20] E. Pehlke, *Phys. Rev. Lett.* **1993**, *71*, 2338.
[21] R. Kraus, *Phys. Rev. B* **2013**, *87*, 134516.
[22] O. Andreussi, *J. Chem. Phys.* **2012**, *136*, 064102.
[23] a) M. Otani, *Phys. Rev. B* **2006**, *73*, 115407; b) N. Bonnet, *Phys. Rev. Lett.* **2012**, *109*, 266101.
[24] H. Bluhm, *J. Phys. Chem. B* **2004**, *108*, 14340.
[25] A. Eilert, *J. Phys. Chem. Lett.* **2017**, *8*, 285.
[26] a) A. Kolmakov, *Nat. Nanotechnol.* **2011**, *6*, 651; b) J. J. Velasco-Velez, *Angew. Chem., Int. Ed.* **2015**, *54*, 14554.
[27] a) L. J. Frevel, *J. Phys. Chem. C* **2019**, *123*, 9146; b) R. Mom, *J. Am. Chem. Soc.* **2019**, *141*, 6537.
[28] a) R. Arrigo, *Angew. Chem., Int. Ed.* **2013**, *52*, 11660; b) H. G. Sanchez Casalongue, *Angew. Chem., Int. Ed.* **2014**, *126*, 7297.
[29] a) Y. Fukai, *Phys. Scripta* **2003**, *2003*, 11; b) Y. Fukai, *Phys. Rev. Lett.* **1994**, *73*, 1640.
[30] a) A. Knop-Gericke, *Top. Catal.* **2001**, *15*, 27; b) M. Favaro, *Proc. Nat. Acad. Sci.* **2017**, *114*, 6706; c) Y. Huang, *ACS Catal.* **2017**, *7*, 1749; d) T. C. Chou, *J. Am. Chem. Soc.* **2020**, *142*, 2857.
[31] J. J. Velasco-Vélez, *J. Phys. Chem. B* **2018**, *122*, 780.
[32] M. C. Biesinger, *Surf. Inter. Anal.* **2017**, *49*, 1325.
[33] a) J. J. Velasco-Vélez, *ACS Sustainable Chem. Eng.* **2018**, *7*, 1485; b) J. J. Velasco-Vélez, *ACS Catal.* **2020**, *10*, 11510.
[34] L. H. Tjeng, *Phys. Rev. Lett.* **1991**, *67*, 501.
[35] a) L. C. Davis, *Phys. Rev. B* **1982**, *25*, 2912; b) A. Tanaka, *J. Phys. Soc. Jpn.* **1994**, *63*, 2788.
[36] L. H. Tjeng, *Phys. Rev. B: Condens. Matter* **1992**, *45*, 8205.
[37] a) A. Föhlisch, *Phys. Rev. Lett.* **2001**, *88*, 027601; b) I. Coulthard, *Phys. Rev. B* **2001**, *64*, 115101.
[38] M. T. Greiner, *Nat. Chem.* **2018**, *10*, 1008.
[39] a) A. P. Graham, *Phys. Rev. B* **1995**, *51*, 5306; b) A. P. Graham, *Phys. Rev. B* **1998**, *57*, 13158; c) H. Matsushima, *J. Am. Chem. Soc.* **2009**, *131*, 10362.
[40] J. J. Velasco-Vélez, *J. Am. Chem. Soc.* **2021**, *143*, 12524.
[41] A. A. Peterson, *Energy Environ. Sci.* **2010**, *3*, 1311.
[42] P. Amann, *Science* **2022**, *376*, 603.
[43] D. Tan, *Nano Lett.* **2022**, *22*, 6298.
[44] C. M. Goodwin, *Nature* **2024**, *635*, 282.